Rapid and Controllable Flame Reduction of TiO₂ Nanowires for Enhanced Solar Water-Splitting

In Sun Cho,[†] Manca Logar,[†,‡] Chi Hwan Lee,[†] Lili Cai,[†] Fritz B. Prinz,[†] and Xiaolin Zheng*,[†]

[†]Department of Mechanical Engineering, Stanford University, California 94305, United States
[‡]Advanced Materials Department, Jozef Stefan Institute, 1000 Ljubljana, Slovenia

S Supporting Information

ABSTRACT: We report a new flame reduction method to generate controllable amount of oxygen vacancies in TiO₂ nanowires that leads to nearly three times improvement in the photoelectrochemical (PEC) water-splitting performance. The flame reduction method has unique advantages of a high temperature (>1000 °C), ultrafast heating rate, tunable reduction environment, and open-atmosphere operation, so it enables rapid formation of oxygen vacancies (less than one minute) without damaging the nanowire morphology and crystallinity and is even applicable to various metal oxides. Significantly, we show that flame reduction greatly improves the saturation photocurrent densities of TiO₂ nanowires (2.7 times higher), α-Fe₂O₃ nanowires (9.4 times higher), ZnO nanowires (2.0 times higher), and BiVO₄ thin film (4.3 times higher) in comparison to untreated control samples for PEC water-splitting applications.

KEYWORDS: Flame reduction, oxygen vacancy, TiO₂ nanowires, conductivity, charge transport/transfer efficiencies, photoelectrochemical water-splitting
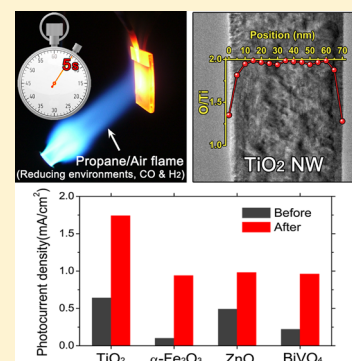
The oxygen vacancy is one of the most important defects in metal oxides, and it can directly affect the surface, electronic, magnetic, dielectric, and electrical properties of metal oxides.[1,2] Oxygen vacancies are often desired for metal oxides to improve their performance for broad applications, ranging from heterogeneous catalysis,[3−5] gas sensors,[6,7] solid−oxide fuel−cell,[8] electronic,[9,10] to electrochemical devices.[11,12] For example, oxygen vacancies at surface serve as adsorption and active sites and strongly influence the surface reactivity,[4,13] so they can enhance the performance of metal oxide based heterogeneous catalysts and gas sensors. Oxygen vacancies also act as electron donors and thereby enhance the electrical conductivity and charge transport property,[14−16] which can improve the performance of field-effect transistors, super-capacitors, and Li-ion batteries.[9,11,17] Specifically for photoelectrochemical (PEC) water-splitting applications, oxygen vacancies were shown to improve both light absorption and charge transport properties of metal oxide photoanodes, leading to an enhanced PEC water-splitting performance.[18,19]

Due to the importance of oxygen vacancy, several reduction methods have been developed to generate oxygen vacancies in metal oxides. One common reduction method is to anneal metal oxides under carbon monoxide (CO),[20] hydrogen (H₂),[18,21,22] or inert gases[5,23] at high temperature. Typically, such gas annealing needs to be conducted either under vacuum conditions or low oxygen pressure to avoid oxygen inclusion so the annealing setup is expensive and sophisticated. Additionally, such gas annealing is carried out below 600 °C to protect the metal oxides and their carrying substrates, so a longer annealing time (>30 min) is needed to generate a sufficient amount of oxygen vacancy. The other common method reduces metal oxides in aqueous solutions using chemically reducing agents (e.g., NaBH₄)[24−26] or electrochemically by applying bias.[27,28] Although solution-based reduction methods conveniently work at atmospheric pressure, their low processing temperature (<100 °C) requires a long reduction time (tens of minutes), and they can induce crystallinity change as well.

Here, we report a simple, rapid, and effective flame reduction method to introduce controllable and tunable amount of oxygen vacancies in metal oxides by using TiO₂ nanowires (NWs) as a model system. Flame has the unique advantages of high temperature (>1000 °C) and an ultrafast heating rate, and it can introduce oxygen vacancies to metal oxides in less than one minute. Such a short treatment time also preserves the morphology and crystallinity of TiO₂ NWs. Significantly, flame reduction greatly improves the photocurrent density of TiO₂ NWs for a PEC water-splitting application, and such improvements are also observed for other flame-reduced metal oxide photoanodes.

Results and Discussion. *Flame Reduction Process and Oxygen Vacancy Characterization.* The flame reduction process of TiO₂ nanowires (NWs) is schematically illustrated in Figure 1a. Rutile TiO₂ NWs with an average length of 3.0 μm and diameter of 100 nm are first grown on fluorine-doped tin oxide (FTO) glass substrates by the hydrothermal method.[29,30]
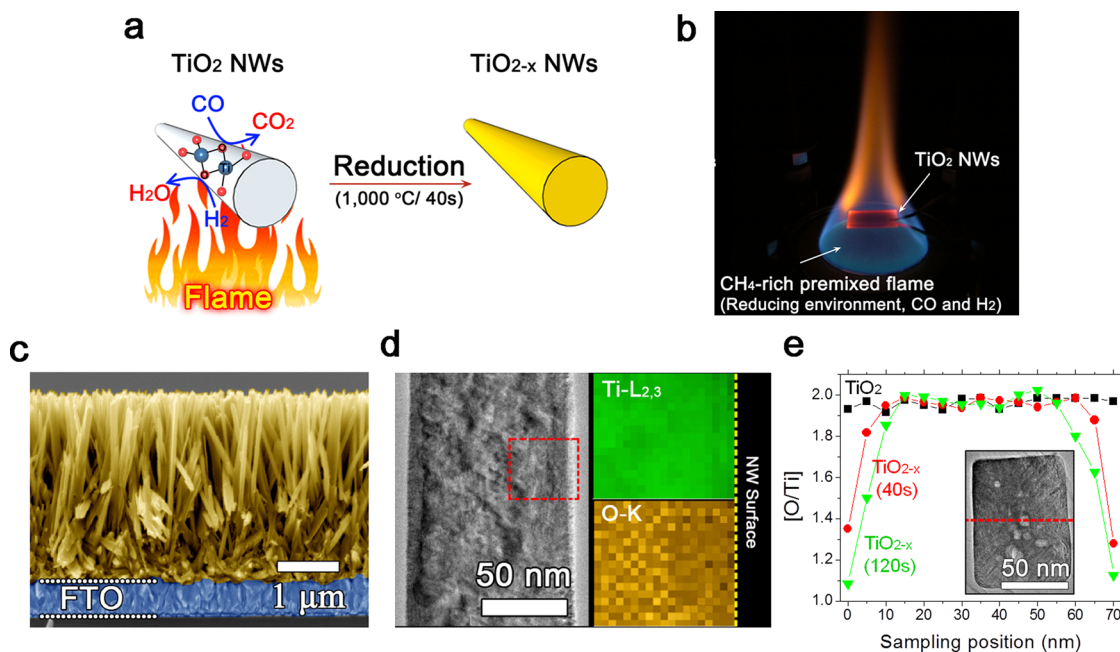
Figure 1. Flame reduction process and characterization of oxygen vacancy distribution. (a) Schematic illustration of the flame reduction method. (b) A photograph of the flame reduction process. (c) A representative cross-sectional SEM image of the flame-reduced TiO_2 NWs. (d) Bright-field STEM image and the corresponding electron energy loss spectroscopy (EELS) elemental mapping of Ti-$L_{2,3}$ and O−K edges inside the rectangular box, showing an oxygen deficiency near the NW surface. Darker color: lower concentration of oxygen. (e) The O/Ti molar ratio distribution along the NW diameter (as-synthesized TiO_2 NW: black rectangles and flame-reduced TiO_2 NWs: red circles: 40 s, green triangles: 120 s), which is estimated using EELS spectra taken from a cross-line shown in the inset of a cross-sectional TEM image. Flame reduction conditions: T = 1000 °C, Φ = 1.4, and t = 40 or 120 s.

Then, the TiO_2 NWs are clamped with tweezers and quickly inserted into the postflame region of a coflow premixed flat flame,[30,31] and the TiO_2 NWs are annealed there with a local gas temperature about 1000 °C for 5−120 s. The coflow premixed flame uses methane (CH_4) as the fuel and air as the oxidizer, and it operates at CH_4-rich and air-deficient conditions to provide a reducing environment that contains high concentrations of CO and H_2 (see the Methods section). Consequently, the TiO_2 NWs are reduced by the flame, forming oxygen vacancies. Our flame reduction method, in comparison to common reduction methods such as H_2 annealing,[11,18,21] electrochemical[27] and metal hydride solution reductions,[24] has several advantages. First, the high temperature and ultrafast heating rate of the flame enables the formation of oxygen vacancies in less than one minute, instead of tens of minutes or even hours as other methods. Such brief high temperature reduction minimizes the morphology and crystallinity change of TiO_2 NWs and prevents the delicate FTO/glass substrate from thermal damage.[30] As shown in Figure 1c and Supporting Information Figures S1−2, the flame-reduced TiO_2 NWs exhibit indistinguishable high crystallinity and morphology as those of as-synthesized TiO_2 NWs. Second, the coflow flat premixed flame configuration (Figure 1b) provides a spatially uniform environment in terms of temperature and gas compositions so that a large size of TiO_2 NWs sample can be reduced uniformly. For example, the diameter of our burner is 6 cm, and we can reduce the 4 cm × 4 cm size sample uniformly. Third, the flame reduction is simple and conducted in an open-atmospheric condition, so it does not require expensive vacuum systems like the H_2 annealing method. Even some ubiquitous flames, such as propane torch flames, can be utilized to reduce TiO_2 NWs (Figure 5). Moreover, the flame reduction is carried out in the gas phase,

and it reduces the chance for impurity incorporation as encountered by the solution phase reduction. Finally, the flame reduction conditions can be conveniently tuned by changing the flame temperature and the flame fuel and air equivalence ratios, allowing the flame reduction method to be applicable to other metal oxide materials, such as α-Fe_2O_3, ZnO and $BiVO_4$, as well.

The formation and distribution of oxygen vacancies in the flame-reduced TiO_2 NWs are analyzed by the electron energy loss spectroscopy (EELS) technique (see the Methods section). As shown in Figure 1d, the EELS elemental mapping of Ti and O at the rectangular region shows that oxygen is deficient near the surface of the flame-reduced TiO_2 NW. The O/Ti molar ratios are further quantitatively examined in cross sections of TiO_2 NWs (Figure 1e). The O/Ti molar ratio is about 2 for the as-synthesized TiO_2 NW as expected, but it decreases below 2 in the outer 10−15 nm layer of the flame-reduced TiO_2 NW and drops to about 1.3 and 1.1 at the surface for 40 s and 120 s reduction, respectively. The EELS results clearly show that oxygen vacancies are successfully generated inside TiO_2 NWs by flame reduction. In addition, the TEM-EDS (energy dispersive spectroscopy) and EELS analysis (Supporting Information, Figure S3) do not show a detectable amount of carbon even for prolonged flame reduction of 120 s, so it suggests that the flame reduction mainly generates oxygen vacancies in the TiO_2 NWs with a negligible amount of carbon impurity incorporation if there is any. The reason for the low carbon incorporation is that CH_4 does not contain C−C bonds and does not tend to form soot. It should be noted that our flame reduction method is different with previous flame treatments used to improve the PEC performance of TiO_2.[32−34] Flames used before are typically Bunsen burner using high sooting-tendency propane and butane as fuels, and
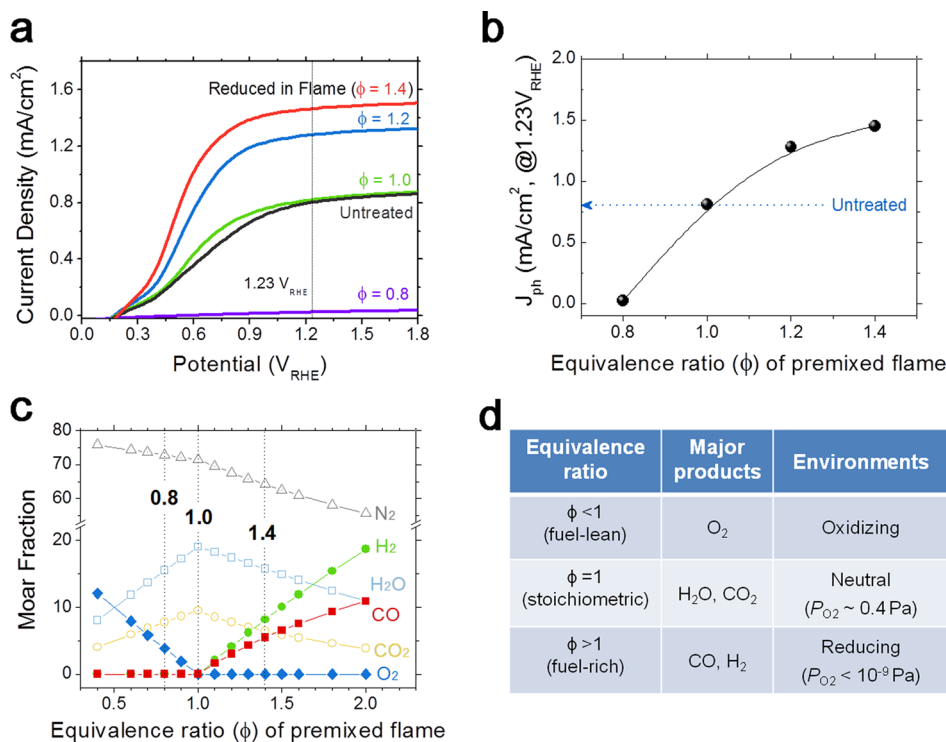
Figure 2. Effect of the fuel-to-air equivalence ratio (Φ) on PEC water-splitting performance of the flame-reduced TiO$_2$ NWs. (a) $J-V$ curves. (b) Photocurrent density values (J_{ph}, at 1.23 V_{RHE}) as a function of equivalence ratio. Flame reduction conditions: T = 1000 °C and t = 60 s. (c) Molar fraction of major gaseous combustion product as a function of equivalence ratio in the postflame region. (d) Effects of equivalence ratio on the flame annealing environments.

they mainly introduce carbon doping and also change the phase and crystallinity of TiO$_2$. Our flame reduction is controlled to generate oxygen vacancy, not carbon doping, while maintaining the phase and crystallinity of TiO$_2$. In addition, our flat premixed flame provides spatially uniform temperature and gas phase compositions in contrast to the highly nonuniform Bunsen burner flames. Hence, with our flame reduction method, we can focus on the effects of oxygen vacancy on the PEC performance of TiO$_2$.

Optimization of Flame Reduction Conditions for PEC Water-Splitting Performance. To optimize the flame reduction conditions of TiO$_2$ NWs, we vary the flame annealing parameters, including the flame fuel-to-air equivalence ratio (Φ) and the flame annealing time and evaluate the properties of TiO$_2$ NWs by applying them as photoanodes for PEC water-splitting. The PEC water-splitting performance of flame-reduced TiO$_2$ NWs is determined by measuring the photo-current−potential ($J-V$) curves using a standard three-electrode configuration under AM1.5G simulated solar light illumination (100 mW/cm^2) (see the Methods section) and compared with those of the as-synthesized (untreated) TiO$_2$ NWs.

(1) Effect of the Flame Fuel-to-Air Equivalence Ratio (Φ). First, the flame fuel-to-air equivalence ratio (Φ) is defined as the actual fuel/oxygen mass ratio normalized by the stoichiometric fuel/oxygen mass ratio (eq 1). Experimentally, the flame equivalence ratio is controlled by adjusting the flow rates of CH$_4$ and air (see the Methods section).

$$ \Phi = \frac{m_{CH_4}/m_{O_2}}{(m_{CH_4}/m_{O_2})_{st}} \tag{1} $$

To focus on the effect of flame equivalence ratio, the flame annealing temperature and time of TiO$_2$ NWs are fixed at 1000 °C (about ±50 °C measurement error) and 60 s, respectively. Figure 2a shows the PEC $J-V$ curves of the TiO$_2$ NWs that are annealed under four different equivalence ratios: Φ = 0.8, 1.0, 1.2 and 1.4, and the corresponding photocurrent density values at 1.23 V_{RHE} ($J_{ph,1.23V}$) are plotted as a function of the equivalence ratio in Figure 2b. After the stoichiometric flame annealing (Φ = 1.0), the TiO$_2$ NWs exhibit nearly identical $J-V$ curves and $J_{ph,1.23V}$ as those of the untreated TiO$_2$ NWs.[30] The TiO$_2$ NWs annealed at the fuel-lean condition (Φ = 0.8) exhibit adversely reduced $J_{ph,1.23V}$ (~0.02 mA/cm^2). On the other hand, the TiO$_2$ NWs annealed at fuel-rich conditions (Φ = 1.2 and 1.4) show significantly improved $J_{ph,1.23V}$.

To understand the effect of flame equivalence ratio on the TiO$_2$ PEC water-splitting performance (photocurrent density values), the gas-phase composition in the postflame region is calculated using the combustion equilibrium calculation code STANJAN (see the Methods section). Figure 2c shows the equilibrium molar fractions of gaseous combustion product species in the postflame region as a function of equivalence ratio. The effect of flame equivalence ratio on the flame annealing environment is summarized in Figure 2d. First, at the stoichiometric condition (Φ = 1.0), mainly neutral (non-reactive) gases, such as H$_2$O and CO$_2$, are present due to complete combustion reaction of CH$_4$/air, which leads to the identical $J-V$ curve and $J_{ph,1.23V}$ for TiO$_2$ NWs after flame annealing. Second, at the fuel-lean condition (Φ < 1.0), O$_2$ is a major product, and it removes the surface defects of the TiO$_2$ NW by oxidation.[23] The removal of surface defect states hinders the water molecules adsorption process, so oxidized TiO$_2$ NWs have worsened PEC performance. Third, at fuel-rich
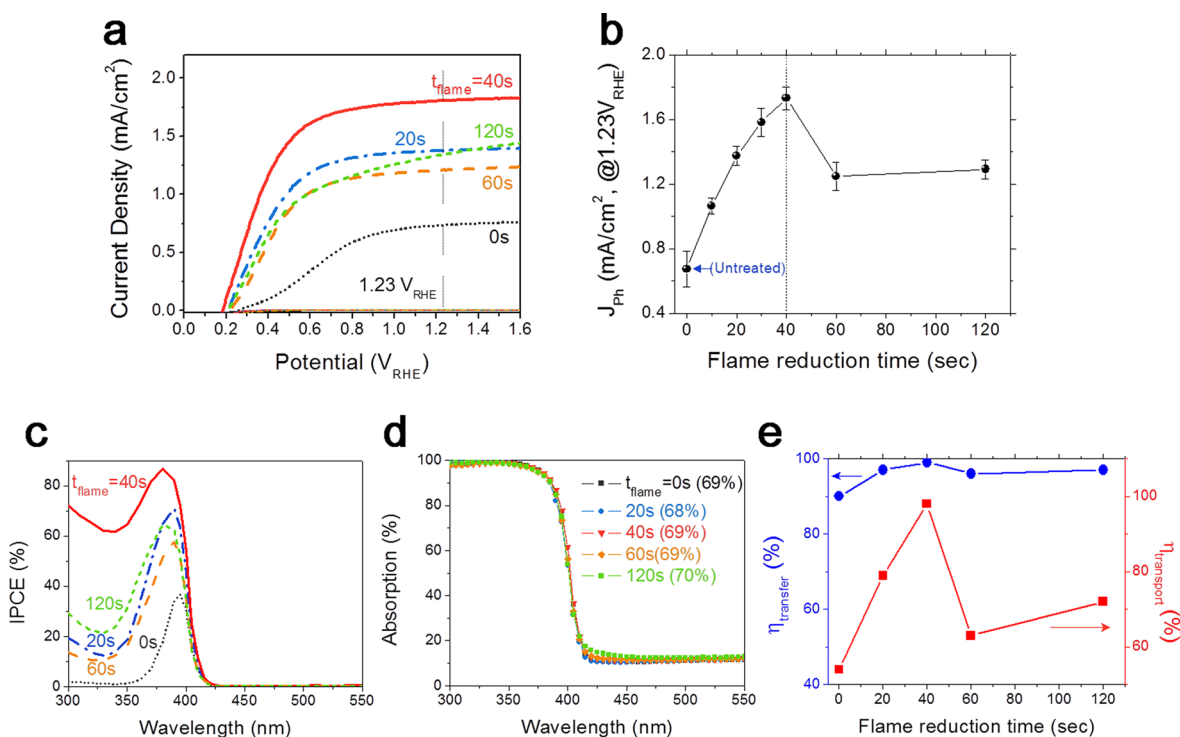
Figure 3. Effect of flame reduction time on PEC water-splitting performance of the flame-reduced TiO_2 NWs and characterization of enhancing factors. (a) J–V curves. (b) Photocurrent density values (at 1.23 V_{RHE}) as a function of flame reduction time. The error bars represent the standard deviation of at least three samples. (c) IPCEs spectra measured at 1.23 V_{RHE}. (d) Light absorption for which TiO_2 NWs grown on transparent quartz substrates are used. Even though the sample reduced for 120 s shows a weak shoulder at 420–460 nm (i.e., sample color changed from white to light-yellow, Supporting Information, Figure S7c), all of the samples show comparable light absorption (68–70%) regardless of the flame reduction time. (e) Charge transfer and charge transport efficiencies (at 1.23 V_{RHE}) as functions of flame reduction time. Flame reduction conditions: T = 1000 °C, and Φ = 1.4.

conditions ($\Phi > 1.0$), reducing gases, H_2 and CO, are major combustion products due to the partial oxidation of CH_4 by air, and there is very little O_2 present. For example, the partial pressure of O_2 (P_{O_2}) is about 1.0×10^{-9} Pa (cf., P_{CO} = 5.6 kPa and P_{H_2} = 8.3 kPa) for Φ = 1.4. Hence, H_2 and CO effectively reduce the TiO_2 NWs by generating oxygen vacancies, leading to improved PEC water-splitting performance.

(2) Flame Reduction Time (t_{flame}). Next, the effect of flame reduction time on the TiO_2 PEC water-splitting performance is evaluated by fixing the flame temperature at 1000 °C and the equivalence ratio Φ at 1.4. Figure 3a shows the representative PEC J–V curves of TiO_2 NWs reduced for different times (0, 20, 40, 60, and 120 s), and the corresponding photocurrent density values at 1.23 V_{RHE} ($J_{ph,1.23V}$) are plotted as a function of the flame reduction time in Figure 3b. For short flame reduction time up to 40 s, the $J_{ph,1.23V}$ increases monotonically with increasing the reduction time. A flame reduction of only 40 s triples the $J_{ph,1.23V}$ from 0.64 mA/cm² for the untreated TiO_2 NWs to 1.74 mA/cm². For longer flame reduction time above 40 s, the $J_{ph,1.23V}$ decreases to about 1.3 mA/cm² for the t_{flame} = 120 s sample, which is still about two times higher than that of the untreated sample. It should be noted that experiments with each flame treatment condition are repeated for three TiO_2 NW samples, and the corresponding J–V curves are highly reproducible with a standard deviation of ∼8% (Supporting Information, Table S1).

To understand the effect of flame reduction time, the wavelength-dependent photocurrent responses are further compared by measuring the incident photon to current

conversion efficiency (IPCE) for the TiO_2 NWs reduced for different time duration (Figure 3c). First, all of the flame-reduced TiO_2 NWs exhibit higher IPCE values than that of the untreated TiO_2 NWs throughout the entire wavelength region below the band gap (∼420 nm). The IPCE values reach the maximum value of 87% when t_{flame} = 40 s. Second, the most prominent improvement of the IPCE values occurs in the shorter wavelength region (<350 nm) for all of the flame-reduced samples. The high energy photons in this shorter wavelength region have a small absorption depth ($1/\alpha$) about a few tens of nanometers (Supporting Information, Table S2), so they are mainly absorbed by the surface layers of TiO_2 NWs which are rich in oxygen vacancies (Figure 1e). In other words, the prominent IPCE improvement in the ultraviolet region is closely related to the addition of oxygen vacancies near the top surface of TiO_2 NWs.

The IPCE of the TiO_2 NW photoanode is determined by the efficiencies of three fundamental processes involved in PEC water-splitting (eq 2), that is, charge generation efficiency ($\eta_{e-/h+}$), charge transport efficiency within the material ($\eta_{transport}$), and charge transfer (collection) efficiency at the electrode/electrolyte interface ($\eta_{transfer}$).[30,35]

$$\text{IPCE} = \eta_{e-/h+} \times \eta_{transport} \times \eta_{transfer} \qquad (2)$$

To identify the key factors responsible for the IPCE improvement in the flame-reduced TiO_2 NWs, the individual contributions of the above three factors are investigated separately. First, the light absorption spectra of the five TiO_2 NW samples with different reduction times are measured and compared over a wavelength range from 300 to 550 nm. As
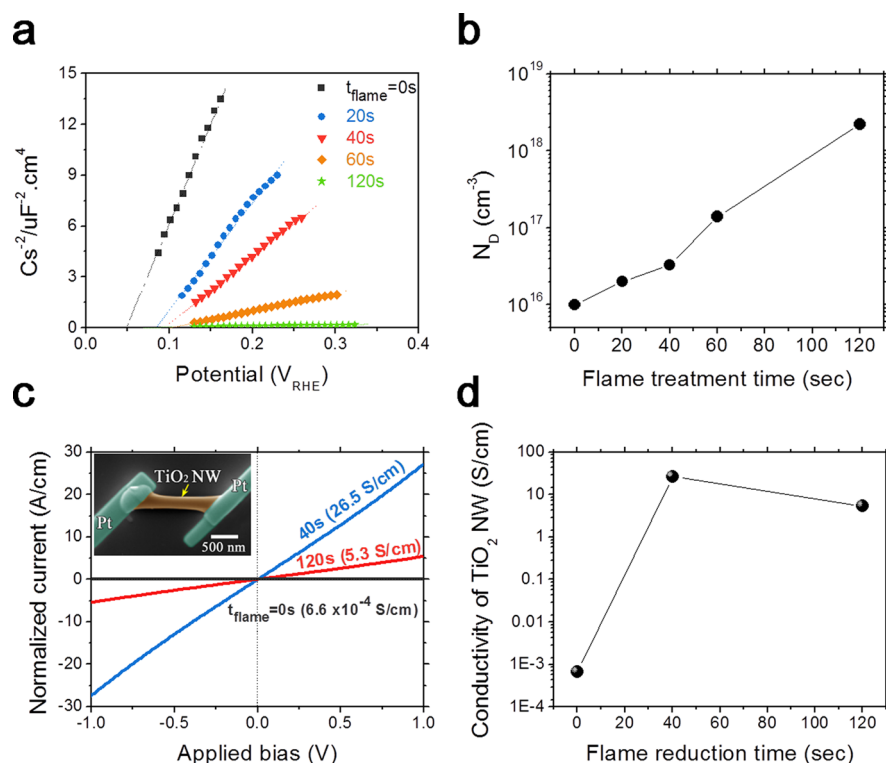
Figure 4. Effects of flame reduction time on the electrical transport properties of TiO$_2$ NWs. (a) Mott−Schottky plots (collected at a frequency of 1 kHz) of TiO$_2$ NWs and (b) the corresponding donor density values. The surface area of NWs film is estimated by the NW coverage density and the average dimensions (length and width) of NWs. (c) Current−potential ($I-V$) curves of single TiO$_2$ NWs (the inset shows an SEM image of a single TiO$_2$ NW with metal (Pt) contacts at both ends used for such measurement) and (d) the corresponding NW conductivity values.

shown in Figure 3d, all of the five samples show comparable light absorption (68−70%) regardless of the flame reduction time, indicating that the flame reduction has little impact on the light absorption and equivalently the charge generation efficiency ($\eta_{e-/h+}$). Second, the charge transfer and transport efficiencies of the five TiO$_2$ NWs are decoupled and quantified by using H$_2$O$_2$ as a hole scavenger (see the Methods section and Supporting Information, Figure S3). As shown in Figure 3e, for the charge transfer efficiency, all of the flame-reduced TiO$_2$ NWs show higher $\eta_{transfer}$ than the untreated sample, and especially the t_{flame} = 40 s sample has the highest $\eta_{transfer}$ of nearly 100%. The observed improvement of $\eta_{transfer}$ for the flame-reduced TiO$_2$ NWs supports the fact that oxygen vacancies formation at the TiO$_2$ surface provides additional active sites for water molecules adsorption,[13,36] thereby enhancing the charge transfer process for oxygen evolution reaction (OER). Nevertheless, the overall $\eta_{transfer}$ improvement is only about 7−10%, which is not large enough to explain the much greater improvement of IPCE and $J_{ph,1.23V}$ with flame reduction. Third, the charge transport efficiency ($\eta_{transport}$) shows the greatest sensitivity toward the flame reduction time. The TiO$_2$ NW sample reduced for 40 s has the highest $\eta_{transport}$ of 98%, twice as high as that of the untreated sample (54%). This result indicates that the flame reduction significantly enhances the $\eta_{transport}$ and through which improves the PEC performance, which is consistent with the observation that the IPCE improvement mainly occurs at the shorter wavelength region.

Next, to further understand this great improvement in the charge transport efficiency by flame reduction, the electron transport properties (e.g., donor density and conductivity) are further compared by measuring the electrochemical impedance

and conductivity of individual TiO$_2$ NWs (Figure 4). The charge carrier (donor) density values estimated from the Mott−Schottky plots (Figure 4a and b) show an exponential increase of donor density with increasing the flame reduction time. The electrical conductivities obtained by measuring individual TiO$_2$ NWs are ∼0.0006, 26.4, and 5.3 S/cm for t_{flame} = 0, 40, and 120 s, respectively (Figure 4c and d). The flame-reduced TiO$_2$ NWs have over 4 orders of magnitude higher conductivity than the untreated TiO$_2$ NW. These results suggest that flame reduction increases the donor concentration and hence improves the overall electron transport property. In addition, although the t_{flame} = 120 s sample has higher donor density than that of the t_{flame} = 40 s sample, its conductivity is about five times lower, indicating that longer flame reduction likely increases the bulk recombination and adversely affects the electron transport property. Finally, it should be noted that prolonged flame treatment will increase the sheet resistance of the FTO film (Supporting Information, Figure S5), which also contributes to the lower $\eta_{transport}$ in the t_{flame} = 120 s sample.

We further compare the PEC water-splitting performance between the optimally reduced TiO$_2$ NWs (flame equivalence ratio = 1.4, temperature = 1000 °C, and t_{flame} = 40 s) and TiO$_2$ NWs reduced by other methods, that is, H$_2$ annealing, NaBH$_4$, and TiCl$_3$ solution methods. The flame-reduced TiO$_2$ NWs sample shows comparable but modestly better PEC water-splitting performance (high photocurrent density and good photocurrent stability) (Supporting Information, Figure S6) than the TiO$_2$ NWs samples reduced by other methods. Additionally, we also compare the flame reduction method with reduction in a common rapid thermal annealing (RTA) system, which has a comparable large heating rate as with flame. Flame reduction is found to be a more effective method than RTA in

reducing TiO$_2$ NWs for improving the PEC performance due to the heating mechanism differences between flame and RTA (Supporting Information, Figure S7). Importantly, the flame reduction method requires the shortest treatment time (40 s instead of 30 min) to obtain optimally reduced TiO$_2$ NWs, and it is simple and scalable.

Versatility of the Flame Reduction Method. The flame reduction method has great versatility in application. The flame reduction process can be accomplished by many flame sources with proper control of the gas phase composition. In addition to the CH$_4$/air flat premixed flame used above, CH$_4$/H$_2$/air flat premixed flames and even premixed propane torch flames (Figure 5, inset) can be used to effectively reduce TiO$_2$ NWs,
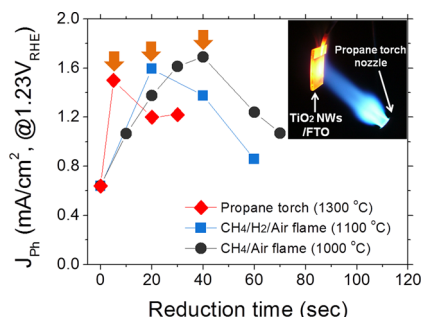

Figure 5. Photocurrent density values versus reduction time of TiO$_2$ NWs reduced by different flame sources, showing that high-temperature flame source shortens the optimal reduction time for achieving the highest J_{ph}. The temperature of flame is measured by inserting a K-type thermocouple into the postflame region for 30 s. The inset photograph shows the reduction process of TiO$_2$ NWs grown on FTO substrate by a propane torch.

leading to greatly enhanced PEC water-splitting performance (Figure 5). Similar to the CH$_4$/air premixed flame, there is an optimal reduction time for TiO$_2$ NWs to maximize the photocurrent density values ($J_{ph,1.23V}$) for both the CH$_4$/H$_2$/air premixed flame and propane torch flames (Figure 5). The optimal reduction time decreases with increasing the flame temperature. Especially, in the case of the propane torch flame at temperature of 1300 °C, only a 5 s flame reduction increases the $J_{ph,1.23V}$ by more than twice. Finally, the flame reduction method can generate oxygen vacancies in diverse metal oxide materials, regardless of their preparation methods. To illustrate this, the similar flame reduction method with the premixed

CH$_4$/air flame is applied to three metal oxide photoanodes: α-Fe$_2$O$_3$ nanorods, ZnO NWs, and BiVO$_4$ film. As shown in Figure 6, the PEC water-splitting performance, that is, both the photocurrent density values and the onset voltage values, of all three samples is significantly improved compared to the untreated samples (Supporting Information, Table S3). In particular, the flame reduction increases the photocurrent density of α-Fe$_2$O$_3$ nanorods by over nine times.

In summary, we report a general flame reduction method to introduce a controllable and tunable amount of oxygen vacancies in TiO$_2$ NWs. Flame reduction significantly improves the PEC water-splitting performance of TiO$_2$ NWs because the generated oxygen vacancies greatly improve the charge transport efficiency by increasing the donor density and facilitate the charge transfer efficiency by providing additional active sites for water adsorption. Comparing to existing reduction methods, the flame reduction method operates at ambient conditions and is rapid (less than a minute) and effective. Even a 5 s reduction by a propane torch flame can double the photocurrent density of TiO$_2$ NWs for the PEC water-splitting application. Flame reduction of α-Fe$_2$O$_3$ nanorods, ZnO NWs, and BiVO$_4$ film also leads to significantly improved PEC performance. We believe that the flame reduction method will become a general and cost-effective way to generate oxygen vacancies in oxide materials, impacting many applications.

Experimental Methods. *Synthesis of Rutile TiO$_2$ NWs.* The pristine TiO$_2$ NW arrays with an average length of 3.0 μm were synthesized on TiO$_2$ nanoparticles coated-FTO (fluorine-doped tin oxide, TEC-8, Pilkington) substrates using the hydrothermal method, and the details were reported in our previous work.[30] Briefly, 0.6 mL of titanium(IV) butoxide (Aldrich Chemicals, 97%) was added into 50 mL of an aqueous HCl solution (25 mL of deionized (DI) water + 25 mL of concentrated HCl (38%)) under magnetic stirring. After stirring for another 5 min, the solution was poured into a Teflon-lined stainless steel autoclave (100 mL capacity), and pieces of the TiO$_2$ nanoparticles coated-FTO substrates were immersed in the solution. The autoclave was sealed and heated to 170 °C in an oven and held at 170 °C for 7 h. The autoclave was then removed from the oven and cooled down to room temperature naturally. The FTO substrates with the top obtained products were washed with DI water and annealed at 500 °C for 1 h in air.
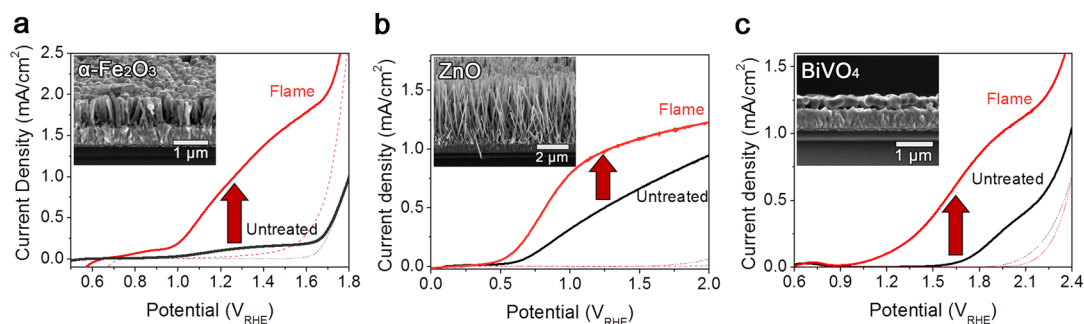

Figure 6. Comparison of PEC $J-V$ curves of other metal oxide photoanodes before/after flame reduction. (a) Hematite (α-Fe$_2$O$_3$) nanorods (1000 °C, Φ = 1.4 and 5 min). (b) ZnO nanowires (1000 °C, Φ = 1.4, 2 min). (c) BiVO$_4$ film (1000 °C, Φ = 1.4, 2 min). Since the oxygen diffusion coefficients of α-Fe$_2$O$_3$ ($\sim10^{-20}$ cm^2/s @ 1100 °C) and ZnO ($\sim10^{-14}$ cm^2/s @ 1100 °C) are much smaller than that of rutile TiO$_2$ ($\sim10^{-7}$ cm^2/s @ 1100 °C), a longer flame reduction time is used. The insets show cross-sectional SEM images of the corresponding samples after flame reduction, showing that there is little change in morphologies after flame reduction.

Flame Reduction Experiments. The flame reduction experiment was conducted using a 6 cm diameter coflow premixed flat flame burner (McKenna Burner) which operates on a premixture gas of CH_4 (fuel) and air (oxidizer).[30,31] The flat premixed flame configuration (Figure 1b) provides a spatially uniform environment in terms of temperature and gas phase species compositions. The flow rates of CH_4 and air were 2.05 and 13.3 SLPM, respectively, yielding an overall fuel-to-oxygen equivalence ratio (Φ) of 1.4. The flow rates were varied to achieve other equivalence ratios. The as-synthesized TiO_2 NWs were annealed in the postflame region with a local gas phase temperature of 1000 °C for 5−120 s. Two other flame sources, that is, the CH_4/H_2/air flame and propane torch (model: TS4000T, Bernz-O-Matic), were also used to reduce the TiO_2 NWs. The CH_4/H_2/air premixed flame ($\Phi = 1.4$) was also achieved with the McKenna burner, and the flow rates of CH_4, H_2, and air were 2.05, 4.64, and 27.5 SLPM, respectively. For the propane torch reduction, the distance between the sample and nozzle was fixed to 5 cm so that the sample is located at a high-temperature region with reducing gas environment. The gas composition in the postflame region was calculated with the combustion equilibrium calculation code STANJAN.[37] We specified that the reactants are at 25 °C and 1 atm, and the combustion products are at 1000 °C and 1 atm and have reached equilibrium.

Material Characterization. The morphologies of as-synthesized and flame-reduced TiO_2 NWs were investigated using scanning electron microscopy (SEM, FEI XL30, Sirion). The crystallinity and oxygen vacancies distribution were investigated using a transmission electron microscope (ETEM, FEI Titan 80-300, 300 kV) equipped with an energy dispersive X-ray spectrometer (EDS) and an electron energy loss spectrometer (EELS) (see the Supporting Information for details). For the optical measurements, TiO_2 NWs were grown on quartz substrates (3 cm × 3 cm) using identical growth conditions. The wavelength-dependent optical absorption properties were obtained with an integrating sphere using a xenon lamp coupled to a monochromator (model QEX7, PV Measurements, Inc.).

Photoelectrochemical Measurements. The photoelectrochemical performance of as-synthesized and flame-reduced TiO_2 NWs was measured with a potentiostat (model SP-200, BioLogic) in a three-electrode configuration (a saturated calomel reference electrode (SCE), TiO_2 working electrode, and a Pt wire counter electrode) under illumination of simulated solar light (AM 1.5G, 100 mW/cm^2) using a solar simulator (model 94306A, class AAA, Oriel). Before measurement, the solar simulator intensity was calibrated with a reference silicon solar cell and a readout meter for solar simulator irradiance (model 91150 V, Newport). The illuminated area of the working TiO_2 electrode was 0.63 cm^2 defined by a mask. For TiO_2 and α-Fe_2O_3 electrodes, 1 M KOH or 1 M KOH with 0.5 M H_2O_2 solution was used as the electrolyte. For ZnO and $BiVO_4$ electrodes, 0.5 M of pH 7 phosphate buffer solution was used as the electrolyte. During the PEC measurement, the electrolyte was deaerated by argon purging to remove the dissolved oxygen. For a typical $J-V$ measurement, the voltage was swept linearly from −1.0 to 2.0 V_{SCE} at a scan rate of 50 mV/s. The electrochemical impedance spectroscopy (EIS) measurements were performed in the same three-electrode configuration with the same potentiostat but under dark conditions The amplitude of the sinusoidal voltage was 10 mV, and the frequency range examined was from 100 kHz to 1 Hz. For the Mott−Schottky analysis, the capacitance values were derived from the EIS measurement, and charge carrier density values were estimated using data sets at 1 kHz. The incident photon-to-current conversion efficiency (IPCE) was measured at 1.23 V_{RHE} ($\sim$0.2 V_{SCE}) using a specially designed IPCE system for solar cell (QEX7, PV measurements), with the three-electrode configuration. A 75 W Xe lamp equipped with a monochromator (CM-110, 1/8, SP Spectra Product) was used to generate a monochromatic beam. The incident light intensity was calibrated by a standard silicon photodiode. The charge transport and transfer efficiencies were estimated as functions of applied potential by using H_2O_2 as a hole scavenger under AM1.5G simulated solar light illumination.[38] The key assumption for this approach is that the oxidation kinetics of H_2O_2 is very fast, and its charge transfer efficiency is 100%, so the ratio of photocurrent density measured in H_2O and H_2O_2 gives the charge transfer efficiency ($\eta_{transfer}$) for H_2O (eq 3). The charge transport efficiency ($\eta_{transport}$) was further calculated by dividing photocurrent density in H_2O_2 by the total light absorption efficiency ($\eta_{e-/h+}$) which is obtained from integration of the light absorption (Figure 3d) with respect to the AM1.5G solar light spectrum (eq 4).

$$\eta_{transfer} = \frac{J_{ph,H_2O}}{J_{ph,H_2O_2}} \tag{3}$$

$$\eta_{transport} = \frac{J_{ph,H_2O_2}}{\eta_{e^-/h^+}} \tag{4}$$

■ ASSOCIATED CONTENT

⑤ Supporting Information

Description of synthesis methods of other metal oxides (Fe_2O_3, ZnO and $BiVO_4$), other reduction methods ($TiCl_3$, $NaBH_4$, and rapid thermal annealing reductions), and more detailed characterizations of the flame-reduced TiO_2 NWs in this work. This material is available free of charge via the Internet at http://pubs.acs.org.

■ AUTHOR INFORMATION

Corresponding Author
*E-mail: xlzheng@stanford.edu.

Notes
The authors declare no competing financial interest.

■ ACKNOWLEDGMENTS

■ REFERENCES

(1) Ganduglia-Pirovano, M. V.; Hofmann, A.; Sauer, J. *Surf. Sci. Rep.* **2007**, *62*, 219.
(2) Pacchioni, G. *ChemPhysChem* **2003**, *4*, 1041.
(3) Queeney, K. T.; Friend, C. M. *J. Phys. Chem. B* **1998**, *102*, 5178.
(4) Polarz, S.; Strunk, J.; Ischenko, V.; van den Berg, M. W. E.; Hinrichsen, O.; Muhler, M.; Driess, M. *Angew. Chem., Int. Ed.* **2006**, *45*, 2965.
(5) Liu, L.; Zhao, C.; Li, Y. *J. Phys. Chem. C* **2012**, *116*, 7904.

(6) Epifani, M.; Prades, J. D.; Comini, E.; Pellicer, E.; Avella, M.; Siciliano, P.; Faglia, G.; Cirera, A.; Scotti, R.; Morazzoni, F.; Morante, J. R. *J. Phys. Chem. C* **2008**, *112*, 19540.

(7) Wang, D.; Sun, J.; Cao, X.; Zhu, Y.; Wang, Q.; Wang, G.; Han, Y.; Lu, G.; Pang, G.; Feng, S. *J. Mater. Chem. A* **2013**, *1*, 8653.

(8) Adler, S. B. *Chem. Rev.* **2004**, *104*, 4791.

(9) Arnold, M. S.; Avouris, P.; Pan, Z. W.; Wang, Z. L. *J. Phys. Chem. B* **2002**, *107*, 659.

(10) Chang, P.-C.; Fan, Z.; Chien, C.-J.; Stichtenoth, D.; Ronning, C.; Lu, J. G. *Appl. Phys. Lett.* **2006**, *89*, 133113.

(11) Shin, J.-Y.; Joo, J. H.; Samuelis, D.; Maier, J. *Chem. Mater.* **2011**, *24*, 543.

(12) Luo, J.-Y.; Chen, L.-J.; Zhao, Y.-J.; He, P.; Xia, Y.-Y. *J. Power Sources* **2009**, *194*, 1075.

(13) Schaub, R.; Thostrup, P.; Lopez, N.; Lægsgaard, E.; Stensgaard, I.; Nørskov, J. K.; Besenbacher, F. *Phys. Rev. Lett.* **2001**, *87*, 266104.

(14) Kubacka, A.; Fernández-García, M.; Colón, G. *Chem. Rev.* **2011**, *112*, 1555.

(15) Nowotny, M. K.; Sheppard, L. R.; Bak, T.; Nowotny, J. *J. Phys. Chem. C* **2008**, *112*, 5275.

(16) Wang, Z. L. *J. Phys.: Condens. Matter* **2004**, *16*, R829.

(17) Lu, X.; Wang, G.; Zhai, T.; Yu, M.; Gan, J.; Tong, Y.; Li, Y. *Nano Lett.* **2012**, *12*, 1690.

(18) Wang, G.; Wang, H.; Ling, Y.; Tang, Y.; Yang, X.; Fitzmorris, R. C.; Wang, C.; Zhang, J. Z.; Li, Y. *Nano Lett.* **2011**, *11*, 3026.

(19) Gan, J.; Lu, X.; Wu, J.; Xie, S.; Zhai, T.; Yu, M.; Zhang, Z.; Mao, Y.; Wang, S. C. I.; Shen, Y.; Tong, Y. *Sci. Rep.* **2013**, *3*.

(20) Wang, X.; Hanson, J. C.; Frenkel, A. I.; Kim, J.-Y.; Rodriguez, J. A. *J. Phys. Chem. B* **2004**, *108*, 13667.

(21) Liu, H.; Ma, H. T.; Li, X. Z.; Li, W. Z.; Wu, M.; Bao, X. H. *Chemosphere* **2003**, *50*, 39.

(22) Rekoske, J. E.; Barteau, M. A. *J. Phys. Chem. B* **1997**, *101*, 1113.

(23) Thompson, T. L.; Yates, J. T., Jr. *Top. Catal.* **2005**, *35*, 197.

(24) Kang, Q.; Cao, J.; Zhang, Y.; Liu, L.; Xu, H.; Ye, J. *J. Mater. Chem. A* **2013**, *1*, 5766.

(25) Manthiram, A.; Dananjay, A.; Zhu, Y. T. *Chem. Mater.* **1994**, *6*, 1601.

(26) Tsang, C.; Lai, S. Y.; Manthiram, A. *Inorg. Chem.* **1997**, *36*, 2206.

(27) Zhonghai, Z.; Hedhili, M. N.; Zhu, H.; Wang, P. *Phys. Chem. Chem. Phys.* **2013**, *15*, 15637−15644.

(28) Lindquist, S.-E.; Lindgren, A.; Leygraf, C. *Sol. Energy Mater.* **1987**, *15*, 367.

(29) Cho, I. S.; Chen, Z.; Forman, A. J.; Kim, D. R.; Rao, P. M.; Jaramillo, T. F.; Zheng, X. *Nano Lett.* **2011**, *11*, 4978.

(30) Cho, I. S.; Lee, C. H.; Feng, Y.; Logar, M.; Rao, P. M.; Cai, L.; Kim, D. R.; Sinclair, R.; Zheng, X. *Nat. Commun.* **2013**, *4*, 1723.

(31) Rao, P. M.; Cho, I. S.; Zheng, X. *Proc. Combust. Inst.* **2013**, *34*, 2187.

(32) Mazare, A.; Paramasivam, I.; Schmidt-Stein, F.; Lee, K.; Demetrescu, I.; Schmuki, P. *Electrochim. Acta* **2012**, *66*, 12.

(33) Shankar, K.; Paulose, M.; Mor, G. K.; Varghese, O. K.; Grimes, C. A. *J. Phys. D: Appl. Phys.* **2005**, *38*, 3543.

(34) Xu, C.; Shaban, Y. A.; Ingler, W. B., Jr.; Khan, S. U. *Sol. Energy Mater. Sol. Cells* **2007**, *91*, 938.

(35) Chen, Z.; Jaramillo, T. F.; Deutsch, T. G.; Kleiman-Shwarsctein, A.; Forman, A. J.; Gaillard, N.; Garland, R.; Takanabe, K.; Heske, C.; Sunkara, M.; McFarland, E. W.; Domen, K.; Miller, E. L.; Turner, J. A.; Dinh, H. N. *J. Mater. Res.* **2010**, *25*, 3.

(36) Linsebigler, A. L.; Lu, G.; Yates, J. T. *Chem. Rev.* **1995**, *95*, 735.

(37) Reynolds, W. *Tech. Rep.* **1986**.

(38) Dotan, H.; Sivula, K.; Gratzel, M.; Rothschild, A.; Warren, S. C. *Energy Environ. Sci.* **2011**, *4*, 958.

■ NOTE ADDED AFTER ASAP PUBLICATION

This Letter was published ASAP on December 4, 2013. Figure S7 in the Supporting Information has been modified. The correct version was published on December 9, 2013.